Article:
Childerhouse, T. orcid.org/0000-0001-9669-3806, Hernández-Nava, E., Tapoglou, N. orcid.org/0000-0001-9126-5407 et al. (4 more authors) (2021) The influence of finish machining depth and hot isostatic pressing on defect distribution and fatigue behaviour of selective electron beam melted Ti-6Al-4V. International Journal of Fatigue, 147. 106169. ISSN 0142-1123

https://doi.org/10.1016/j.ijfatigue.2021.106169

The influence of finish machining depth and hot isostatic pressing on defect distribution and fatigue behaviour of selective electron beam melted Ti-6Al-4V

Thomas Childerhouse[a,b,*], Everth Hernández-Nava[a], Nikolaos Tapoglou[c], Rachid M'Saoubi[d], Luiz Franca[e], Wayne Leahy[e], Martin Jackson[a]

[a]*Department of Materials Science and Engineering, University of Sheffield, Sir Robert Hadfield Building, Mappin Street, Sheffield, S1 3JD, UK*
[b]*Industrial Doctoral Centre in Machining Science, Advanced Manufacturing Research Centre with Boeing, University of Sheffield, Rotherham, S60 5TZ, UK*
[c]*Advanced Manufacturing Research Centre with Boeing, University of Sheffield, Rotherham, S60 5TZ, UK*
[d]*Materials & Technology Development, Seco Tools AB, SE73782, Fagersta, Sweden*
[e]*Element Six Global Innovation Centre, Fermi Avenue, Harwell, OX11 0QR, UK*

Abstract

Porosity related defects within metal additive manufactured components has made it challenging to certify their use in fatigue critical applications. In this study, the fatigue behaviour of selective electron beam melted (SEBM) Ti-6Al-4V specimens following hot isostatic pressing (HIP'ing) and finish machining has been investigated. Employing a sufficient material removal depth during machining was shown to significantly improve fatigue performance. This was attributed to be a direct result of removing material rich in lack-of-fusion defects, concentrated in the sub-surface. HIP'ing was shown to enhance fatigue performance to a lesser degree, as the treatment was only effective at reducing gas porosity.

Keywords:
Additive manufacturing, near net shape manufacturing, powder metallurgy, titanium alloys

1. Introduction

Metal additive manufacturing (AM) refers to a group of emerging technologies which offer manufacturers capabilities of directly fabricating components to high levels of geometric precision and intricacy [1, 2]. For the manufacture of titanium alloy components, AM processes are particularity attractive, as their near net shape (NNS) manufacturing capabilities offer the potential for significant cost savings compared to traditional process routes by reducing machining requirements and improving material utilisation rates [3, 4]. For the aerospace industry, the adoption of AM has the potential to offer significant economic benefits and reduce the weight of aircraft through topological optimisation of component geometries [5, 6]. However, limitations concerning the fatigue performance properties of components produced by AM has made it challenging to certify components for their use in fatigue critical applications [7].

Selective electron beam melting (SEBM) is a powder bed technology developed by Arcam AB which utilises an electron beam heat source to consolidate a powder feedstock material by the sequential melting of layers of powder [8]. Powder is melted selectively, based on a cross sectional geometry taken from a CAD file of the component, by scanning a focused electron beam spot to generate a molten pool of material, which quickly solidifies to result in a consolidated part. To focus the beam spot, a series of electromagnetic lenses are used which facilitates rapid scanning velocities. This capability has enabled machine manufacturers to design innovative beam scanning strategies which can achieve active melting at multiple locations simultaneously [9].

The main limitations of components fabricated by powder bed fusion techniques include: (i) a poor surface finish [10], (ii) form error of geometrically critical features [11, 12], and (iii) limited and highly variable fatigue performance [7, 13]. The surface finish of as-built components has been characterised to consist of partially consolidated powder particles that penetrate to depths up to 300 μm, depending on the orientation of the surface relative to the build direction [14]. The poor surface finish of directly fabricated surfaces has motivated research into a number of non-conventional finishing techniques suited for the removal of small material volumes from complex surface geometries. Such techniques include: abrasive flow machining [15, 16], chemical etching/polishing [17], and laser polishing [18]. These techniques offer advantages compared to conventional machining processes as they offer better access to hard to reach features, do not require the programming of complex CNC tool paths, and require more straight forward workholding solutions. However, these processes are not capable at eliminating form error and ensuring that geometric tolerances are met. For component features where functionality is dependent on such tolerances, material removal by either a conventional machining or grinding process remains to be a necessary post processing step.

Regarding the mechanical properties of Ti-6Al-4V consolidated by SEBM, static properties such as the yield and ulti-

*Corresponding author
Email address: tchilderhouse1@sheffield.ac.uk (Thomas Childerhouse)

mate tensile strength have been reported to be similar to those of wrought material [19–21]. In contrast, the fatigue performance of the material has been found to be consistently lower and more variable than that of wrought Ti-6Al-4V. The limited fatigue performance of SEBM Ti-6Al-4V samples has been found to be linked to poor crack initiation resistance of the material, owing to stress concentration sites occurring both at the rough as-built part surface [7, 13], as well as at porosity related defects located below the surface of the material [7]. In machined samples, fatigue failure has been found to occur with cracks nucleating from pores in the sub-surface [7, 22], as well as at pores located initially in the as-built material's sub-surface, but exposed at the newly generated surface following machining [13, 23]. Pores observed in SEBM Ti-6Al-4V have been characterised as being either spherical or irregular in shape. Spherical pores have been attributed to residual argon gas from the powder atomisation process entrapped within individual powder particles and irregular shaped pores have been attributed to lack of fusion between powder particles [24]. Hot isostatic pressing (HIP'ing) has been demonstrated to be an effective process for improving the fatigue performance of SEBM Ti-6Al-4V samples by the closing of internal pores [7, 25, 26]. Additionally, the heat treatment effects of HIP'ing has been found to result in "microstructural coarsening" which has also been reported to improve fatigue behaviour by increasing crack propagation resistance [22, 27].

X-ray computed tomography (XCT) is a technique which has been used to characterise pore morphology, size, and spatial distribution in Ti-6Al-4V samples produced by SEBM. Using the technique, Cunningham et al. [24] have reported an average spherical pore diameter under 10 μm and observed a reduction in the number of pores when employing slower scanning speeds. Tammas-Williams et al. [28] reported that spherical pores contributed to the majority (97%) of the overall pore volume fraction. These were found to be predominantly distributed within material consolidated by the *hatching* scanning melt strategy, used to consolidate the interior region of the build, rather than in material at the boundary of the part consolidated by the *contouring* strategy. The effect of scanning strategy on pore distribution was attributed to be influenced by beam speed, whereby the higher beam speeds employed during hatching result in smaller melt pool sizes and more rapid solidification rates which provide less opportunity for entrapped gas to escape. In another study by the same authors [23], the deleterious effects of porosity on fatigue behaviour was investigated, revealing that defects which were most harmful to fatigue life were those in closest proximity to the surface, particularly those exposed at the surface during machining. Additionally, pore size, aspect ratio, and the proximity of neighbouring pores were all found to influence the stress concentration generated by an individual pore. This preliminary research suggests that the material removal depth employed during post-build machining has the potential to have a significant effect on fatigue performance, as this will influence the proximity of defects relative to the component's surface post-machining.

Stock allowance is a term used to refer to the amount of additional material intentionally included on a part to be removed by finishing techniques to produce the final component. For precision NNS manufacturing processes such as powder bed AM, reducing the stock allowance to the lowest practicable amount is desirable from an economic standpoint [4]. Prior research regarding the fatigue properties of SEBM Ti-6Al-4V has not considered the importance of stock allowance and the manufacture of test specimens has typically involved machining away over 8 mm of material from the as-built part [22, 23, 29]. The present study aims to qualify the influence of stock allowance on the fatigue behaviour of SEBM and HIP'ed SEBM Ti-6Al-4V by removing material at depths less than 1 mm. The removal of material in this range has enabled the fatigue assessment to focus on the region of the build where porosity distribution displays the most heterogeneity. Furthermore, the stock allowance settings used are more typical of those which would be employed in an industrial setting for the manufacture of components consolidated by SEBM.

2. Method and materials

2.1. Specimen fabrication

The fatigue test specimens analysed in this study were fabricated at the University of Sheffield from Ti-6Al-4V pre-alloyed plasma atomised powder using the Arcam Q20 plus SEBM system implementing software version 5.2.52. The feedstock material was provided by Arcam AB with a reported particle size distribution of 45 to 106 μm in diameter. Further confirmation of in-spec material was carried out confirming an oxygen content below 0.150 wt.% and in accordance to ASTM standard F2924-14 [30]. All specimens analysed in this study were fabricated in the same orientation during a single build and the CAD input geometry for each specimen was $5.2 \times 20.6 \times 120.0$ mm. A schematic representation of the build configuration is given in Fig. 1a showing specimens positioned in a 6×10 array, with individual specimens spaced 5 mm apart. An example of an as-built test specimen is shown in Fig. 1d.

Fabrication of the test specimens was carried out following the standard Arcam operating procedures and employing standard parameter settings for the beam scanning strategy, which are further discussed in the literature [9, 28]. Prior to powder deposition, the system was stabilised at vacuum conditions ($<2 \times 10^{-3}$ mBar) controlled by backfilling with helium, to reduce any potential for oxidation of the powder during processing. The process cycle then involved preheating the stainless steel build plate to 500 °C, followed by the application of a 90 μm powder layer over the build area. The deposited powder was then preheated using a defocused beam spot (+60 mA offset) to initiate sintering of the powder to improve its electrical conductivity as well as to maintain an overall elevated processing temperature. Following preheating, consolidation of the powder was carried out using Arcam's default melt strategy employing a sharper beam spot (+45 mA offset). The standard melt strategy consists of two unique beam scanning stages. The initial stage, referred to as *contouring* (Fig. 1b), involves scanning the beam around the perimeter of the cross-section to melt the boundary of the part. This is followed by the *hatching* strategy (Fig. 1c), used to consolidate the interior region of powder.

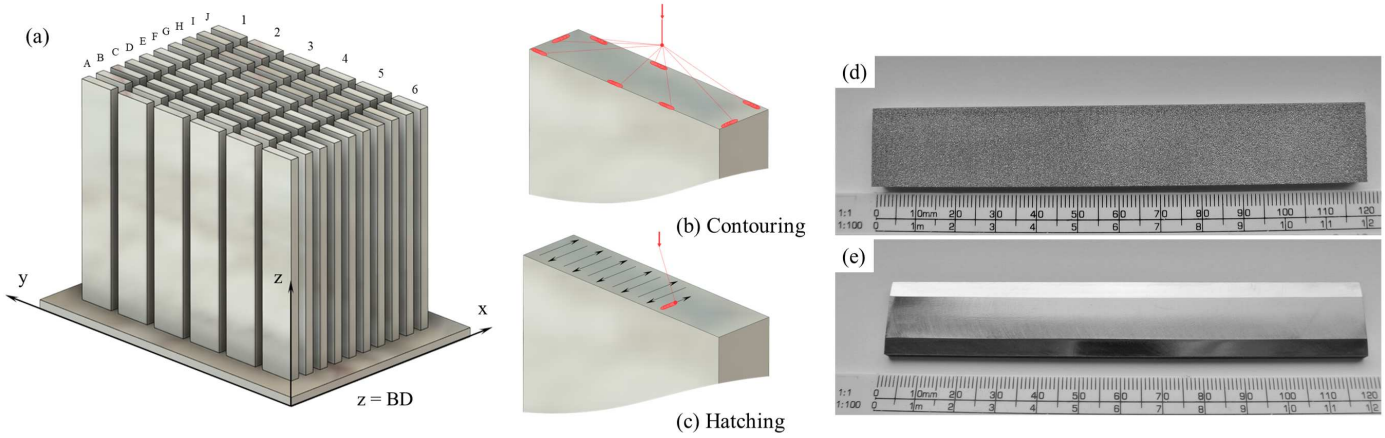

Figure 1: Build schematic for specimen fabrication by the SEBM process - (**a**) shows the CAD build file and the scanning strategies for the respective *contouring* and *hatching* stages are shown in (**b**) and (**c**). The build direction is denoted by the z-direction and hatching carried out with beam motion in the x and y axes. Specimens in the as-built and post-machined conditions are shown in (**d**) and (**e**) respectively.

Whereas *contouring* employs slower beam speeds for improving the parts geometric accuracy and surface finish, *hatching* employs significantly higher beam speeds to reduce the overall processing time. For the specimens fabricated for this study, a two pass *contouring* process was carried out with the default line offset setting of 0.27 mm to consolidate the external 0.80 mm periphery of each specimen. During both preheating and *contouring* stages, Arcam's *MultiBeam* function was employed to enable active heating/melting at multiple locations simultaneously by rapid point-to-point movement of the beam spot. For the *hatching* stage, a continuous beam path was used following a bi-directional raster scanning path as shown in Fig. 1c. During *hatching*, a line offset of 0.18 mm was employed and the scanning direction was alternated by 90° for the consolidation of sequential powder layers. Demanded beam speed during *hatching* was not predefined, but adapted by the control software implementing Arcam's *AutoCalculation* compensations which alter the beam speed for a given beam current to maintain a consistent melt pool size. This process sequence of powder application, pre-heating, and melting was then repeated using the default layer thickness of 90 µm for the Q20 system up until completion of the build.

2.2. HIP processing

The HIP treatment was carried out prior to machining using an AIP8-45H system. Specimens were held at respective conditions of 100 MPa and 920 °C for pressure and temperature in an Argon filled chamber for a two hour duration and cooled to room conditions at a rate of 6 ± 2 °C/min. These conditions are similar to those used in previous studies [25, 31, 32] and within the recommended range suggested by ASTM standard F2924 [30]. The chemical composition of the samples in the pre and post-HIP condition are given in Table 1.

2.3. Finish machining

Post-build finish machining was carried out for all specimens to achieve the final test piece shown in Fig. 1e. Specimens were machined to respective dimensions of 3.6, 19.0, and 120 mm for height (h), width (w) and length (l) (Fig. 2a) and featured a chamfer angle (θ) of 10° to generate a test surface of 10 mm in width. To investigate the influence of stock allowance, this test surface was machined at two different conditions. For the first condition, material was removed to a depth of 0.50 mm relative to the original as-built surface and for the second condition a total depth of 1.00 mm was removed. By employing these two material removal depths, machined test surfaces were generated within the region of the build consolidated by both the *contouring* and *hatching* melt strategies. Additionally, specimens were also tested without undergoing any machining of this test surface to assess the performance of the material in its as-built condition. In addition to the machining of the test surfaces, the reverse surface in the X-Z plane and two surfaces in the Y-Z planes (Fig. 2a) were also machined to eliminate any potential stress concentration at non-test surfaces resulting from the as-built surface.

Machining was carried out using a DMG Mori DMU EVO 40 machining centre. Specimen test surfaces were machined employing a face milling operation of respective dimensions of 19.0 and 0.50 mm for radial (a_e) and axial (a_p) cutter engagement. The cutter followed a linear tool path with the cutter feed direction denoted by the Z-direction in Fig. 2a. A radial offset distance (Δe) between the cutter and specimen centres was maintained at 2.00 mm. To achieve the two machining depth conditions, specimens were machined by either a single or two pass operation with the purpose of maintaining identical cutting conditions for the finishing pass. This was to ensure that

Table 1: Chemical composition of the Ti-6Al-4V SEBM fatigue specimens used in this work. All measurements given in wt.%. H content was < 10 ppm for all conditions.

	Al	V	C	Fe	O	N	Ti
UD Rolled	5.88	4.10	0.007	0.25	0.21	0.03	Bal.
SEBM	5.68	3.64	0.019	0.23	0.15	0.02	Bal.
SEBM + HIP	5.75	4.01	0.016	0.22	0.15	0.02	Bal.

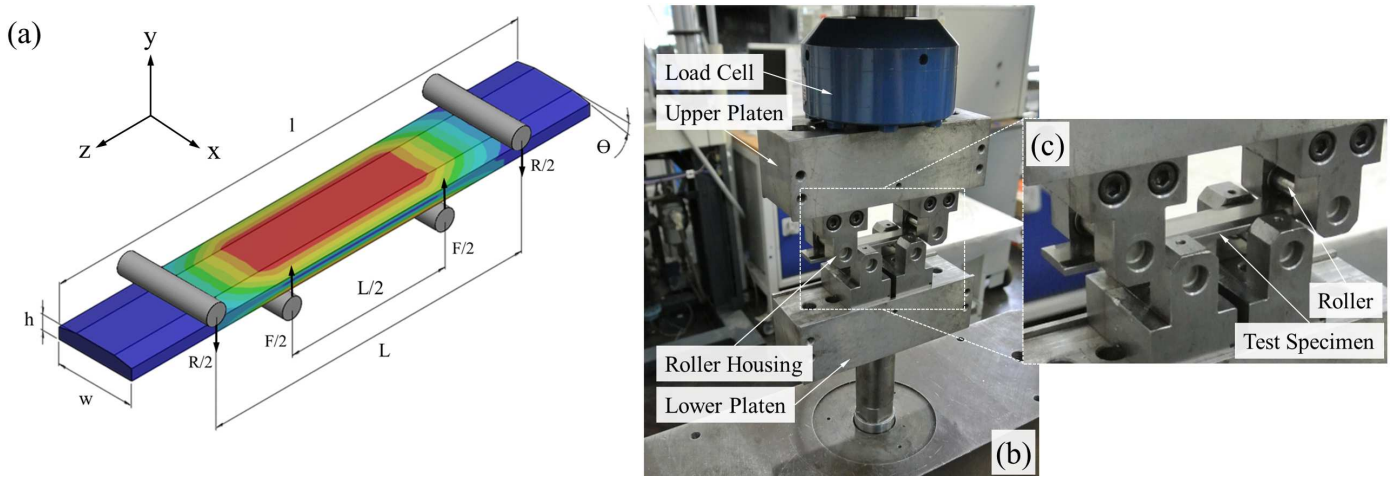

Figure 2: Four point bend test method used to assess fatigue performance - (**a**) schematic representation of the test method and specimen geometry with superimposed FEA stress distribution. (**b**) Annotated photograph of the four point bend test rig at the University of Sheffield and (**c**) a close-up image of a specimen loaded in the test machine.

any variation in surface integrity and fatigue behaviour between the two specimen conditions could be attributed exclusively to the effects of material removal depth. Cutting parameters were maintained at constant settings of 48 m/min and 0.15 mm/tooth for surface speed (V_c) and feed (f_z) respectively. The tooling setup was supplied by Seco Tools and consisted of a 25 mm diameter square shoulder four point indexable milling cutter installed in a HSK-A63 shrinkfit holder. PVD coated carbide inserts were used featuring a TiAlN-TiN PVD coating. During all machining operations, Blaser Swisslube Vasco 7000 cutting fluid was supplied via through tool delivery at a concentration of 5-8%.

2.4. Four point bend fatigue testing

Fatigue testing was carried out with specimens subject to four point bend loading conditions as shown by Fig. 2a. In this configuration, specimens are subjected to a large region of tensile stress concentrated at the test surface as shown by the stress contour map generated by Ansys FE software (Fig. 2a). The selection of the four point bend configuration, rather than a conventional uni-axial setup, has been made to exaggerate the influence of any defects present which are in close proximity to the test surface. Such loading conditions are typical for many titanium alloy components used in fatigue critical aerospace applications and, under such conditions, the presence and location of defects will be critical to performance. This technique has also been used previously to study the influence of machining induced damage on the fatigue behaviour of Ti-5553 [33] and the influence of crystallographic texture resulting from upstream forging on the fatigue behaviour of Ti-6246 [34].

Fatigue testing was carried out at ambient conditions using a Nene 12 kN servo-hydraulic test machine, controlled via a Moog Smartest One controller receiving feedback from a load cell. The four point bend test fatigue setup is shown in Fig. 2b. In this arrangement, dynamic loading was applied to the specimen and distributed through a pair of lower rollers, with the specimen supported by a pair of upper static rollers at a span distance, L = 80 mm. Each test was carried out until the point of failure, with specimens loaded under sinusoidal conditions at a frequency of 5 Hz. For each test, specimens were subjected to a constant maximum stress, S_{Max}, with a number of tests carried out with S_{Max} in the 550 - 750 MPa range. A stress ratio of R = 0.1 was used for all tests.

In addition to the SEBM specimens tested, comparison with conventionally processed counterparts has been carried out using coupons taken from uni-directionally (UD) rolled Ti-6Al-4V plate stock supplied by Rolls-Royce. Coupons were extracted from the stock material in a single orientation by a wire electric discharge machining (wire-EDM) profiling process and then machined to identical specifications used for the SEBM material. UD rolled specimens were tested under higher stress conditions, with S_{Max} in the 750 - 1050 MPa range, owing to their higher performance.

2.5. Characterisation techniques

The assessment of the fracture surfaces and machined surface topographies included in this study was carried out by confocal microscopy using an Alicona InfiniteFocusSL optical 3D measurement system. Large area imaging of the machined surfaces was carried out at ×5 magnification using the stitching function to combine adjacent scans into a single image. Macrograph images of specimen fracture surfaces also employed the stitching function at ×10 magnification. Higher magnification images of individual fracture features were taken at ×20 magnification. To analyse the spatial distribution of lack-of-fusion (LOF) defects on specimen fracture surfaces, the location and size of individual unmelted powder particles were obtained from confocal macrographs using a circle detection image processing function in MATLAB [35]. Images were processed with a resolution of 4 µm to a single pixel and the size threshold limits for individual circle detection was set at 50 - 100 µm, corresponding to the size distribution measured for the starting powder feedstock.

The Vickers microhardness distribution of the specimens prior to machining was characterised using a Struers Durascan 70 with an applied load of 5 kgf (HV 5). Indentations were taken at five positions along a profile in the x-direction in the x-y plane (Fig. 2a. Average microhardness values for material in the non-HIP'ed and HIP'ed conditions was 328 and 309 HV, showing a reduction in hardness following the treatment, which has been attributed to microstructural coarsening in previous studies [20]. The standard deviation in microhardness along the profile was 2% for pre and post-HIP'ed material, indicating minimal variation through the specimen thickness.

3. Results

3.1. Surface assessment

Confocal microscopy images showing the surface topography of machined and as-built SEBM specimen test surfaces are shown in Fig. 3. For each surface presented, corresponding roughness metrics for arithmetical mean height (S_a), root mean square height (S_q), skewness (S_{sk}), and kurtosis (S_{ku}) are given. The HIP treatment was not found to have a significant effect on the surface topography when compared to the non-HIP'ed condition and therefore images of these surfaces have not been included. The as-built surface condition (Fig. 3a) is comprised of a 280 µm layer of partially sintered powder particles. Comparing the surfaces generated for the UD rolled and SEBM material give similar, or improved, roughness metrics for the SEBM material when a 0.50 mm material removal depth has been employed, indicating that machining to this depth has been sufficient to remove the partially consolidated as-built part surface completely.

Analysis of the SEBM surfaces machined to the two different depth conditions reveals the presence of exposed cavities on the newly generated surface when a total stock of 1.00 mm was removed during machining. These were present on the machined surfaces of all 6 non-HIP'ed and on 3 of 4 HIP'ed specimens. Conversely, the machined surfaces generated when employing a material removal depth of 0.50 mm were defect free. An example of a machined surface containing exposed surface defects is shown in Fig. 3b. The topography map height range indicates the depth of penetration of individual defects and shows a penetration depth for the single defect highlighted in the figure to be 180 µm from the machined surface. A higher magnification image of this surface defect is shown in Fig. 3c and shows a cavity with an irregular shaped morphology, containing multiple unmelted powder particles which have failed to be consolidated during the melt stages. This is suggestive that the cavities present on the surface of the specimens are LOF defects which have been exposed during machining.

The effects of defect exposure on the areal surface roughness metrics are evident when comparisons are made between the SEBM material machined at the 0.50 and 1.00 mm conditions. Defect exposure has resulted in an increase in S_a and S_q metrics indicating an increase in roughness. The high negative S_{sk} metric highlights that the roughness increase can be at-

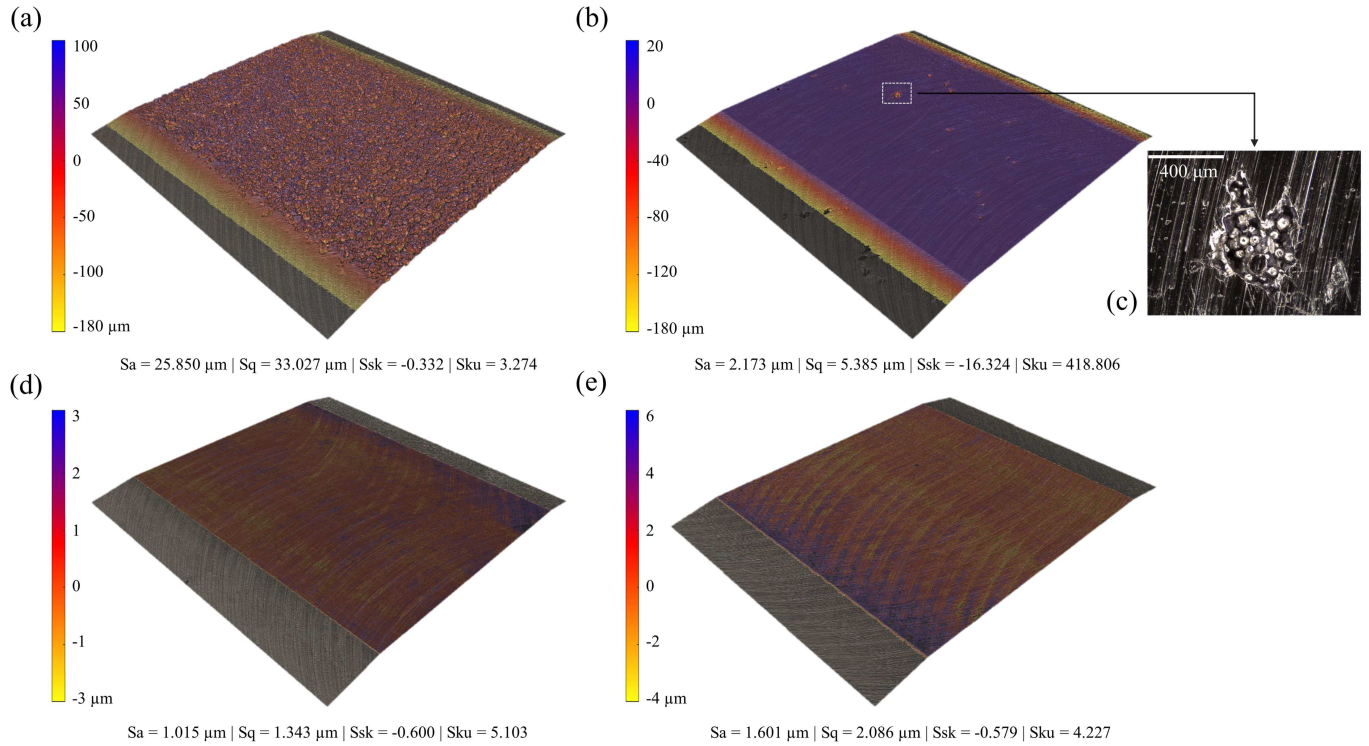

Figure 3: Confocal microscopy images showing the surface topography of non-HIP'ed SEBM specimen test surfaces - (**a**) surface in as-built condition, (**b**) surface machined to a depth of 1.00 mm resulting in exposed defects (**c**) a single LOF pore exposed during machining, (**d**) surface machined to a depth of 0.50 mm. (**e**) Shows the topography of a UD-rolled specimen machined to a depth of 0.50 mm.

tributed to the presence of the cavities, which predominantly lie bellow the nominal machined surface height. Finally the significant increase in the S_{ku} metric indicates the presence of sharp extremities in the surface topography which can be attributed to the presence of LOF within the exposed cavities.

3.2. Fatigue behaviour

Fatigue cycles to failure data for the specimens tested in this study are presented in the S-N diagram given in Fig. 4a. Each specimen was tested to the point of failure with fracture of each specimen occurring in the maximum stress region shown in Fig. 2a. Failure of SEBM specimens occurred within the low cycle fatigue range (LCF) with failure of HIP'ed and non-HIP'ed specimens occurring in the 1,821 to 21,463 and 940 to 11,776 cycle ranges respectively. The fatigue performance of UD rolled material was superior with failure at S_{Max} = 750 MPa exceeding 5×10^5 cycles and failure in the LCF range ($<10^5$ cycles) occurring when $S_{Max} > 1025$ MPa.

To compare the results across the whole applied stress range, the mean normalised cycles to failure value μ for each specimen condition tested has been calculated using Eq. 1. Where n is the number of specimens tested for a given condition, N_{ij} is the cycles to failure for specimen i tested at a single stress level j, and $N_{j,Max}$ and $N_{j,Min}$ are the respective maximum and minimum cycles to failure achieved for a given stress level across all of the specimen conditions.

$$\mu = \frac{1}{n} \sum_{j=1}^{m} \sum_{i=1}^{n_j} \frac{N_{ij} - N_{j,Min}}{N_{j,Max} - N_{j,Min}} \tag{1}$$

The mean normalised data are shown in Fig. 4b. Comparison between the specimens machined at the different stock allowance conditions shows a significant performance increase when 1.00 mm of material was removed, with HIP'ed material enduring on average 69% more cycles prior to failure than those in the as-built condition and non-HIP'ed material enduring over 100% more cycles. A similar performance improvement is not observable for specimens machined to a depth of only 0.50 mm, which achieved on average fewer cycles than their as-built counterparts. Following HIP, the average cycles to failure increased for specimens at each machining condition. This was most evident for specimens which had undergone machining to a 1.00 mm depth, which achieved on average 67% more cycles than their non-HIP'ed counterparts. In addition to the increase in cycles to failure, specimens machined at the 1.00 mm depth condition also display significantly less scatter (10 and 27% for the respective HIP'ed and non-HIP'ed specimens) than those in the other two conditions (> 60%).

3.3. Fractography

Macrographs of the fracture surfaces of specimens in the non-HIP'ed and HIP'ed conditions are shown in Figs. 5 and 6 respectively. Surfaces of specimens in the as-built condition, as well as those machined to a depth of 0.50 mm, show large areas of unconsolidated powder particles which are located predominantly in the sub-surface region and this is evident in both HIP'ed and non-HIP'ed material. Cracks can be seen to initiate at these LOF defects (Fig. 5iii and Fig. 6i and ii) and propagate through the remaining bulk material in the plane perpendicular to the principle stress direction. In Fig. 5a-b and Fig. 6a-b cracks also can be seen to propagate through neighbouring regions of unconsolidated material. In specimens machined to a 1.00 mm depth, the level of unconsolidated material observed for specimens in the prior two conditions is less severe. In this condition, the sub-surface and bulk regions are mostly fully consolidated and LOF defects appear predominantly exposed at the machined test surface. Cracks can be seen to initiate both at the machined surface (Fig. 5iv and Fig. 6iii) and from surface exposed LOF defects (Fig. 6iv). A final observation was the presence of spherical gas porosity, which was visible on the fracture surfaces of non-HIP'ed specimens (Fig. 5ii), but not apparent on the fracture surfaces of specimens having undergone the HIP treatment.

The approximate stress intensity factor, $K_{1,Max}$ associated with a defect subject to mode I can be evaluated using the $\sqrt{area}$ model (Eq. 2) proposed by Murakami [36]. Whereby, the $\sqrt{area}$ parameter is defined by the square root of the projected defect area on a plane perpendicular to the applied principle stress (i.e. the X-Y plane). The parameter C_1 is 0.65 in the case of surface exposed defects and 0.5 for sub-surface, or internal, defects and σ_0 is the maximum stress applied at the defect.

$$K_{1,Max} = C_1 * \sigma_0 * \sqrt{\pi \sqrt{area}} \tag{2}$$

Table 2 gives a summary of the crack size and associated stress intensity factor evaluated using Eq. 2 for the most harmful defects identified at crack initiation sites on the fracture surfaces. The defect area has been calculated based on their approximate elliptical geometry (Fig. 7). A correlation between a reduction in stress intensity factor and an increased fatigue life is shown (Fig. 8), which can be attributed to the reduction in defect area at 1.00 mm machining depths. The affect of the proximity of the critical defect to the surface is also prevalent. For example, the critical defect size for specimens C6 and G6 is similar, however the surface exposure of the defect in specimen G6 has resulted in reduced fatigue performance. For specimens machined to 1.00 mm, the deleterious effects of defect exposure has been less significant on fatigue life than the benefits resulting from a reduction in their size.

3.4. Spatial distribution of defects

The spatial distribution of the LOF defect population on specimen fracture surfaces was analysed using a circle detection image processing function in MATLAB. Unconsolidated powder particles present on the fracture surfaces are presented in Fig. 9 and their distribution in the y-direction from the specimen test surface is shown in Fig. 10. Areas of the build consolidated by either the *hatching* or *contouring* melt strategies are shown by the two shaded areas. The total area fraction of LOF defects present on each fracture surface relative to the overall cross sectional area for specimens in each condition tested are

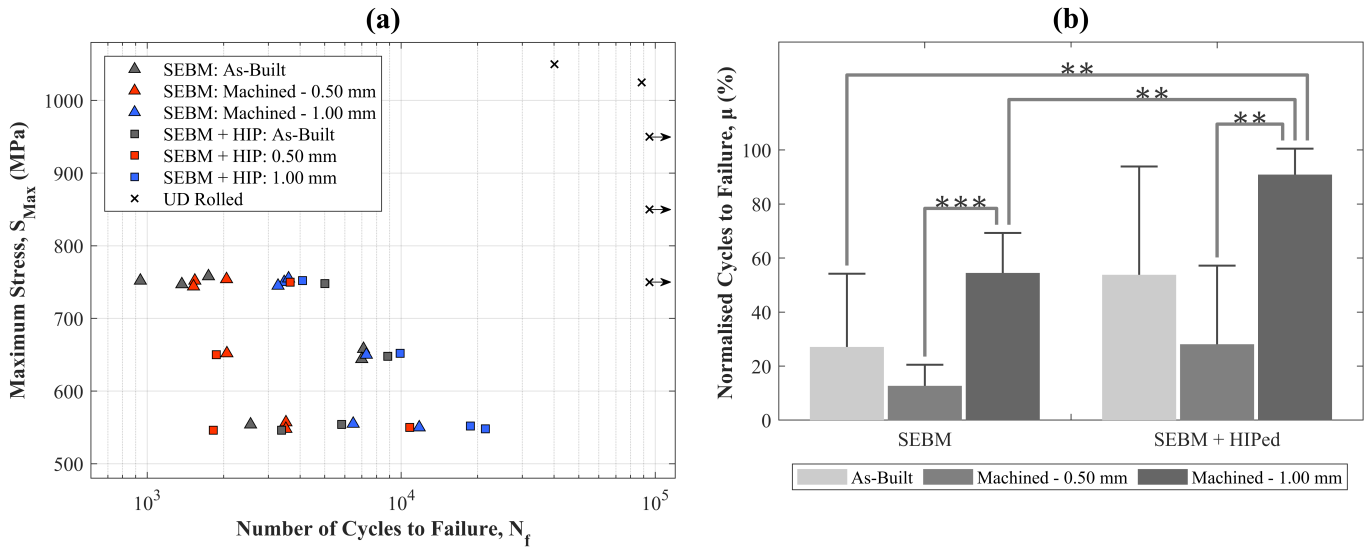

Figure 4: The fatigue performance of SEBM specimens investigated in the study - (**a**) S-N data for HIP'ed and non-HIP'ed SEBM specimens tested compared to specimens machined from conventional wrought (UD rolled) material and (**b**) normalised cycles to failure data for HIP'ed and non-HIP'ed SEBM specimens machined at each stock allowance condition (*** indicates a significant difference $p < 0.001$, ** $p < 0.01$). The error bars shown represent ±1 standard deviation.

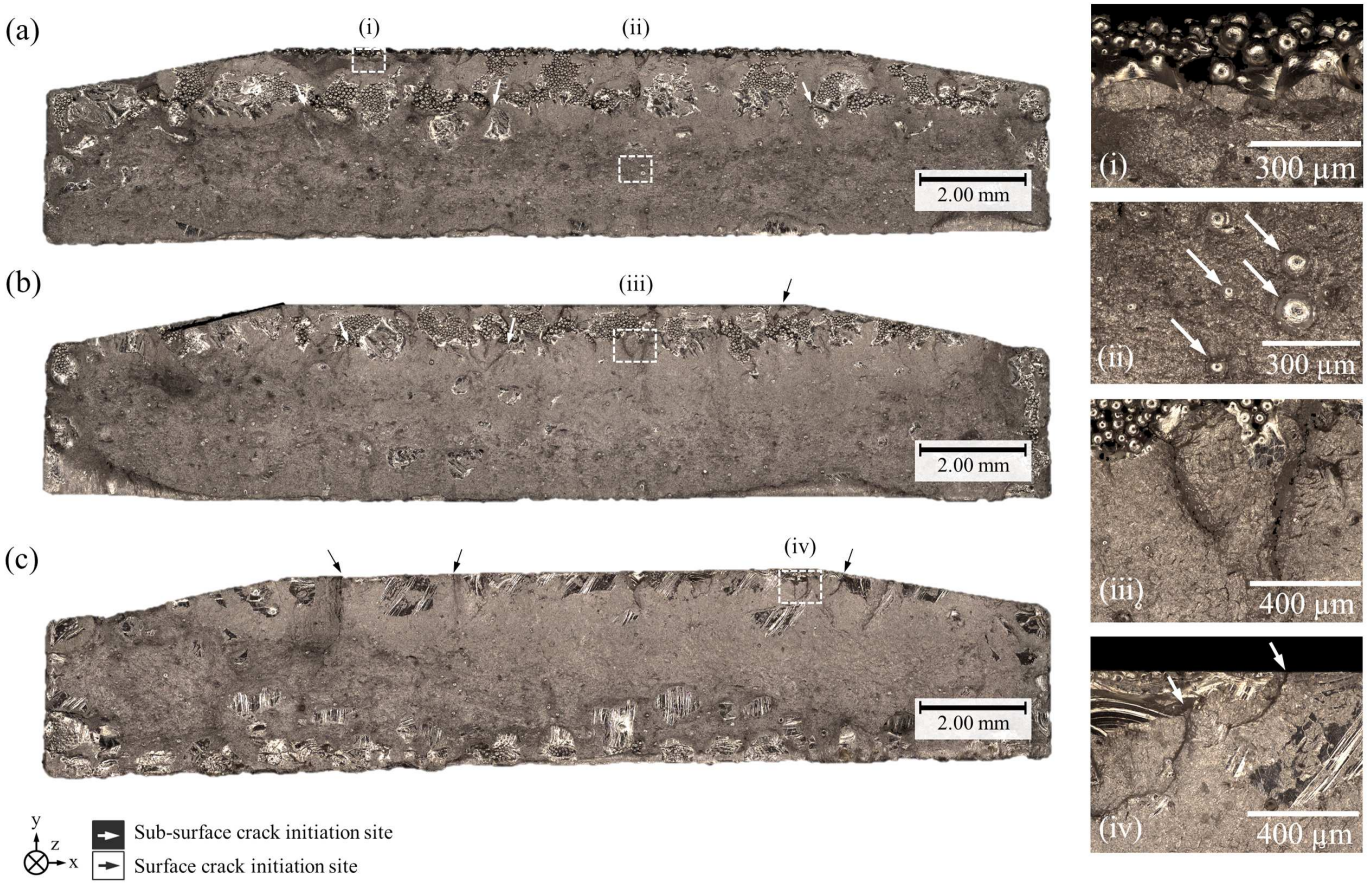

Figure 5: Confocal microscopy images showing example fracture surfaces of non-HIP'ed SEBM specimens - (**a**) shows a macrograph of specimen J2 with the test surface in its as-built condition, (**b**) shows specimen H2 machined to a depth of 0.50 mm, and (**c**) specimen H4 machined to a depth of 1.00 mm. (**i**)-(**iv**) Show higher magnification images images of individual fracture surface features - (**i**) the as-built specimen surface comprised of an external layer of partially melted powder particles, and (**ii**) gas entrapped pores present in the bulk of the specimen. (**iii**) Shows crack initiation at a sub-surface LOF defect, and (**iv**) crack initiation at the machined surface.

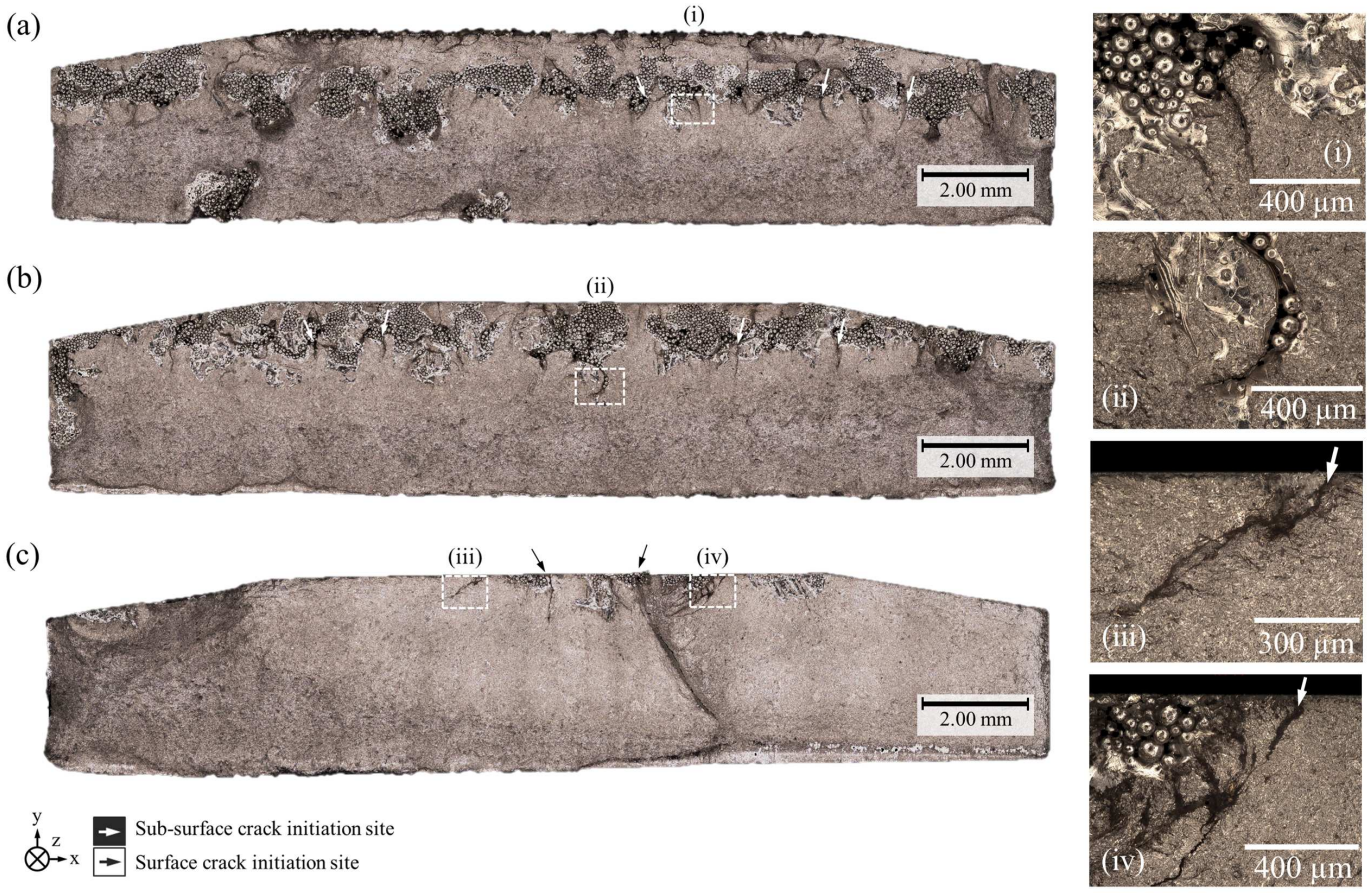

Figure 6: Confocal microscopy images showing example fracture surfaces of HIP'ed SEBM specimens - (**a**) shows a macrograph of specimen C6 with the test surface in its as-built condition, (**b**) shows specimen G6 machined to a depth of 0.50 mm, and (**c**) specimen E1 machined to a depth of 1.00 mm. (**i**)-(**iv**) Show higher magnification images images of individual fracture surface features - (**i**) - (**ii**) show crack initiation at sub-surface LOF defects, (**iii**) shows crack initiation at the machined surface, and (**iv**) shows crack initiation near a surface exposed LOF defect.

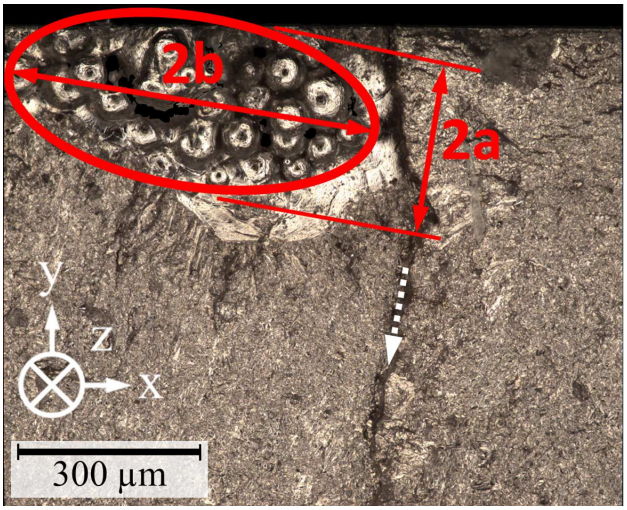

Figure 7: Charaterisation technique used to quantify defect size at crack initiation sites based on approximate elliptical geometry of dimensions *a,b*. Crack propagation direction is indicated by the dotted white arrow. (Fracture surface shown is HIP'ed specimen E1, machined to a depth of 1.00 mm)

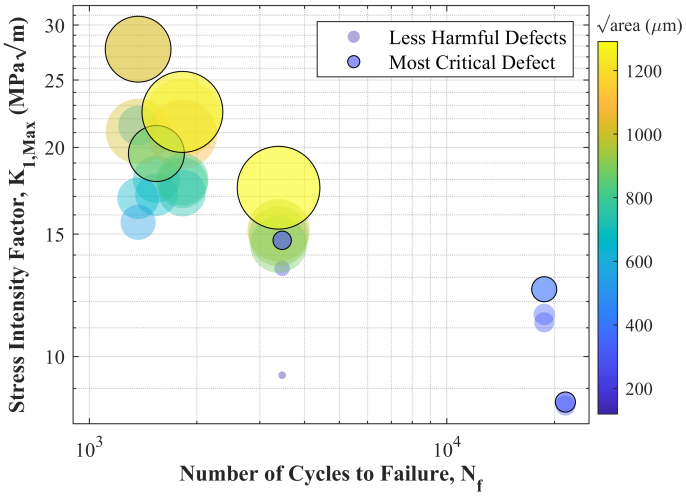

Figure 8: Correlation between fatigue cycles to failure data and stress intensity factor evaluated using Murakami's model [36] (Eq. 2). Marker area shown is proportional to measured defect area.

Table 2: Summary of defect size and the corresponding approximated stress intensity factor for the defects evaluated as most harmful at crack initiation sites.

Sample & ID	Stock allce. (mm)	Crack initiation site	Defect area $\sqrt{area}$ (μm)	Applied stress σ_0 (MPa)	Stress intensity factor $K_{1,Max}$ (MPa $\sqrt{m}$)	Cycles to failure N_f
J2[a]	As-built	Surface exposed LOF[†]	1027	750	27.7	1369
H2[a]	0.50	Sub-surface LOF[†]	873		19.6	1540
H4[a]	1.00	Surface exposed LOF	288		14.7	3462
C6[b]	As-built	Sub-surface LOF[†]	1291	550	17.5	3383
G6[b]	0.50	Surface exposed LOF[†]	1263		22.5	1821
E1[b]	1.00	Surface exposed LOF	391		12.5	18726
F5[b]	1.00	Sub-surface LOF	314		8.6	21463

[a] SEBM, [b] SEBM + HIP. [†] Indicates crack has propagated through neigbouring defects sites as well as through the specimen thickness.

presented in Table 3. A similar distribution of the LOF defect population can be seen for samples in both the non-HIP'ed condition, as well as those which had undergone HIP treatment. For specimens which had undergone no finish machining, two peaks are clearly distinguishable. The first is located at the surface and corresponds to the partially sintered surface layer (Fig. 5i) which penetrates to a depth of 250 μm from the as-built component surface. The second, more prominent, peak is located in the sub-surface, at a depth of approximately 1 mm from the as-built surface, just below the interface of material consolidated by the *hatching* and *contouring* melt strategies. For material having undergone finish machining to a 0.50 mm depth, a single peak can be observed at a depth of approximately 500 μm, at a similar location relative to the interface of material consolidated by the two melt strategies. In specimens machined to a depth of 1.00 mm, the high concentration of LOF defects in the material's sub-surface observed for the previous two conditions has been removed. This has resulted in a reduced overall volume of defects in the remaining material, with the remaining defects reduced in size and mostly present as exposed cavities at the upper surface of the specimen.

4. Discussion

4.1. The influence of machining stock allowance on defect population and fatigue behaviour

The fatigue performance of the SEBM specimens tested in this study is dominated by the high stress concentration arising at LOF defect sites. Under these conditions, crack initiation will have occurred during the early stress cycles and the fatigue performance will be dominated by the crack propagation stages [37]. Based on the fracture surfaces presented, the fatigue performance can be attributed predominantly to the size and distribution of LOF defects remaining in the material post-machining. Defect rich material can be seen to be concentrated in a band of material in the sub-surface of the as-built test pieces. Stress concentration at these defects has resulted in early onset crack initiation with the crack propagation rate influenced by the stress intensity factor associated with the critical defect size. In specimens which had undergone no post-build machining, as well as those machined to a depth of only 0.50 mm, crack propagation has occurred both through the bulk of the material, as well as between neighbouring regions of unconsolidated material. This has also contributed to low crack growth resistance. Furthermore, large areas of unconsolidated material has resulted in a reduced load bearing cross sectional area, contributing to a further increase in the stress concentration at individual defect sites.

The findings highlight the implications of stock allowance selection on the fatigue properties of SEBM components when subject to post-build finish machining. The concentration of LOF defects in the sub-surface has meant that by machining to a depth of 1.00 mm, the majority of defect rich material has been removed. This has resulted in a reduced number of defects, with the most harmful of those reduced in size (Table 2). In specimens machined at these conditions, lower extremities of LOF defects present in the sub-surface were exposed on the newly machined surface. Despite the poor surface condition, the fatigue life has been improved due to the reduced stress intensity at defects, which is expected to have contributed to a slower crack propagation rate. Additional machining to remove material to a total depth of 1.50 - 2.00 mm from the as-built part surface would be sufficient to remove this defect rich band of material entirely. This could offer a further improvement in fatigue performance, as well as result in a defect free machined surface. In contrast, in specimens machined to a depth of only 0.50 mm, the defect rich band of material was below the layer of material removed during machining. For specimens in this condition, there was no evident improvement in fatigue properties. LOF defects were brought in closer proximity to the specimen test surface, which may have resulted in a detrimental effect on performance, as suggested by the reduction in the average normalised cycles to failure when compared to non-machined specimens. This is likely to be a result of the more harmful effect of the defects present, as they are located within a region of higher stress.

The high degree of scatter in fatigue life for the non-machined and material machined to a 0.50 mm depth can be attributed to the high density of LOF defects present. Variation in the specific location, volume, and geometry of defects present on a part-by-part basis may be contributing to the scatter observed. In contrast, the performance of specimens containing a lower overall defect volume following machining to a 1.00 mm depth is more consistent.

Surface exposed defects were detected when machining at

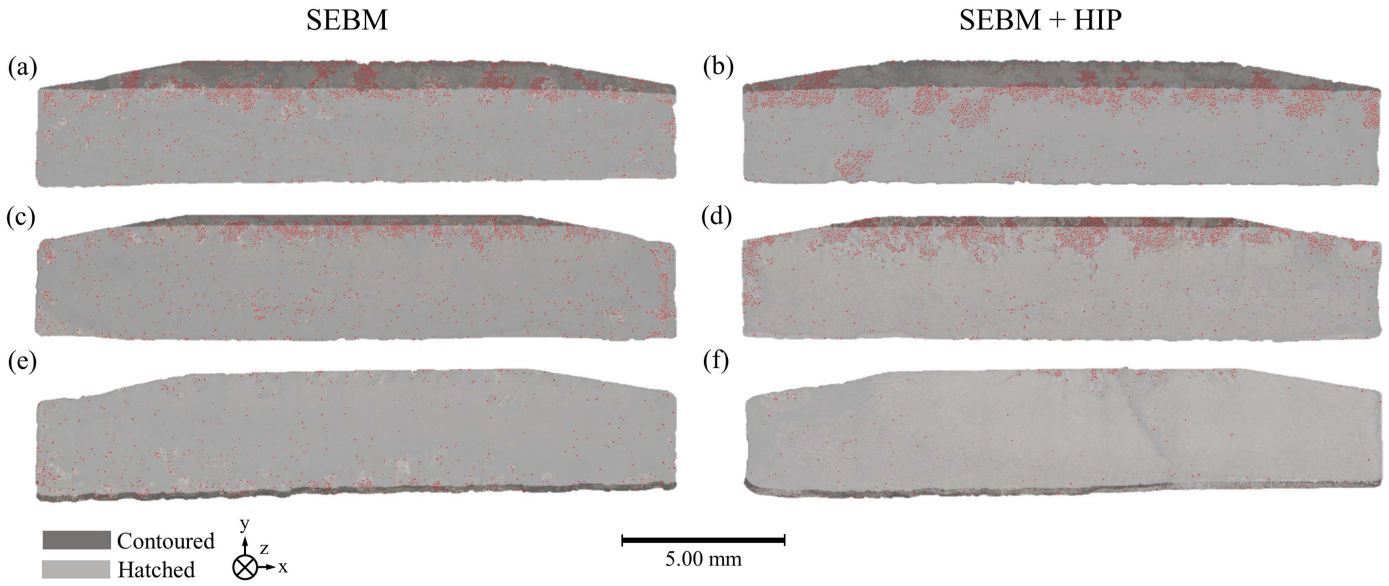

Figure 9: Fractographs of HIP'ed and non-HIP'ed SEBM specimens with regions unconsolidated powder particles detected on the fracture surface superimposed in red - (**a-b**) show specimens with the test surface in its as-built condition, (**c-d**) show specimens with the test surfaces machined to a depth of 0.50 mm, and (**e-f**) show specimens with the test surfaces machined to a depth of 1.00 mm.

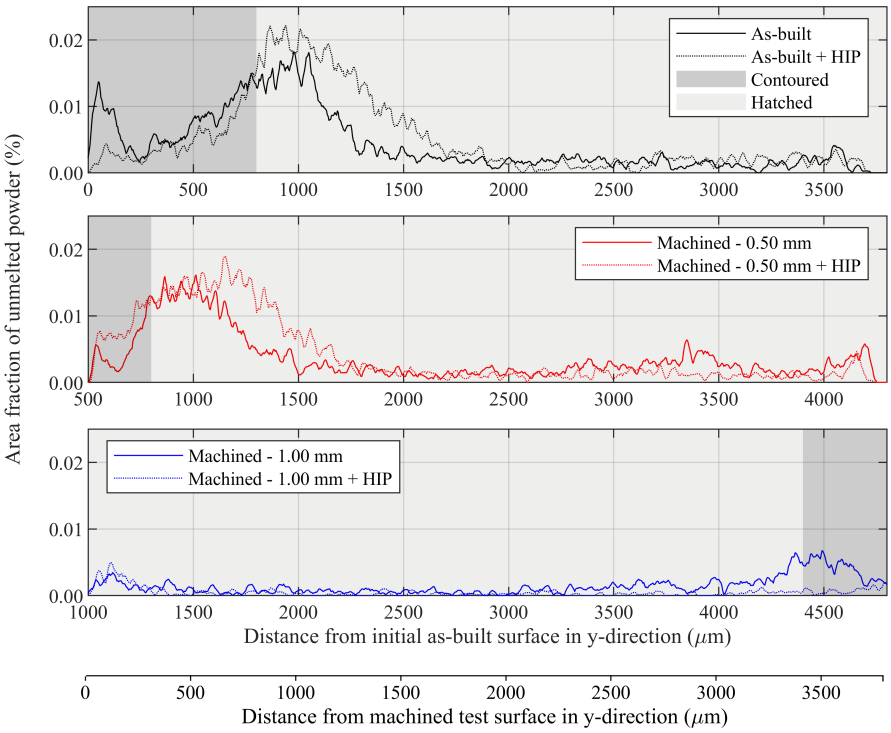

Figure 10: Spatial distribution of the LOF defect population detected on the specimen fracture surfaces shown in Fig. 9. Distribution is shown in the y-direction from the specimen test surface.

Table 3: Summary of fatigue cycle data for both HIP'ed and non-HIP'ed SEBM specimens with the corresponding area fraction of LOF defects identified on the specimen fracture surface given as the percentage of the area of partially or unmelted powder particles in relation to the overall specimen cross sectional area.

Sample ID	Process	Stock allce. (mm)	Peak stress, S_{Max} (MPa)	Cycles to failure, N_f	Area fraction of LOF defects (%)
J2	SEBM	As-built	750	1369	4.04
H2		0.50		1540	3.46
H4		1.00		3462	1.43
C6	SEBM + HIP	As-built	550	3383	4.84
G6		0.50		1821	3.99
E1		1.00		18726	0.50

1.00 mm due a high density in their distribution in this region of the build, whereas at 0.50 mm, the distribution is much lower (Fig. 10) and defect exposure was not observed. Despite this, LOF in this region, can be seen in some instances, such as on the fracture surfaces of specimen J2 (Fig. 5a), and specimens C6, and G6 (Figs. 5a and b). A possible reason for being unable to detect defect exposure for the 0.50 mm condition, could be that LOF has penetrated through fewer layers of the build in this region due to more optimised melt parameters applied by the contouring strategy. This has resulted in defects either remaining sub-surface, or those which have been exposed, presenting with an area lower than the detectable limit.

Although finish machining has been demonstrated to be an effective method at removing most of the defect rich material, this necessitates additional stock removal and limits the material utilisation efficiency offered by SEBM, which is one of the main advantages of precision NNS manufacturing processes, such as powder bed AM. Reducing the number of contouring passes may be an effective method for pushing the lack-of-fusion defects closer to the as-built part surface, as the hatched boundary of the material will be closer to the surface of the workpiece. For example, a single pass contouring strategy (rather than the default two passes) could potentially reduce the penetration depth of LOF defects from the as-built surface. Further modifications to the default scanning strategy whereby the scanning strategy is modified for different component features could also be advantageous. For example, part features which would require post-build machining could be produced using only the *hatching* strategy, as the poor surface finish would be improved following machining. Elsewhere, additional contouring passes could be employed to push defects deeper beneath the part surface, thereby reducing their harmful effect.

4.2. The influence of HIP on defect population and fatigue behaviour

The ineffectiveness of HIP at consolidating unmelted powder particles post-build is evident based on the LOF defects present on the fracture surfaces. A similar spatial distribution of these defects can be seen for material in both the HIP'ed and as-built condition. Specimens which had undergone HIP'ing displayed a similar fatigue performance response to machining depth as non-HIP'ed material. It is noteworthy that an increase in the average fatigue cycles to failure was observed for HIP'ed material. This improvement is most evident in specimens machined at the 1.00 mm condition and can be attributed to the reduction in the volume of gas porosity. In specimens machined to this condition, gas pores contributed to a greater proportion of the overall defect population, due to the reduced level of LOF porosity following machining. Therefore in these specimens, the benefits of HIP has been most evident.

Previous studies [7, 22, 38] have shown an improvement in the fatigue properties of machined specimens following HIP due to a reduction in gas pore size. In these instances, LOF has been considerably less significant than that observed in the present work. Although HIP'ing has been shown to be effective at healing LOF defects of a similar size to those in the present work [25], those with surface connected ligaments fail to be closed as they are filled with high pressure argon during the treatment. This could explain the ineffectiveness of HIP at reducing the LOF defects such as those seen in Figs. 5a and 6a which are surface connected. Additionally, the high density of LOF in this region of the build could have facilitated argon infiltration between neighbouring defects through connected ligaments. It is possible that the HIP treatment has been successful in healing LOF further below the surface, however at the shallow machining conditions employed such defects have been less critical on fatigue failure due to their location in a lower stress region. The limitations of HIP at closing surface connected LOF suggests that that employing sufficient material removal depths (1.50 - 2.00 mm) could result in their removal following machining. At this condition, HIP could provide a more significant fatigue improvement as residual LOF located deeper in the part would have been healed.

4.3. The influence of scanning parameters on defect population

Compared to preceding research the defects observed in the present study are much more severe. Defects observed in builds using earlier tungsten filament based SEBM systems such as the Arcam A2X [22] and S12 [28] were found to be predominately gas pores, rather than the LOF defects observed in the present study utilising the cathode based Q20 plus system. Based on the consistent band-like distribution of the LOF defects observed, it is evident that the spatial distribution of unconsolidated material is related to the beam scanning strategy employed. Defects are located predominantly in the region of material consolidated by the *hatching* strategy and are concentrated towards the interface of material consolidated by the *hatching* and *contouring* strategies. This location corresponds with the position where the beam turns the corner at the end of each hatched pass. During *hatching*, the beam speed is increased as it turns the corner at the end of each pass based on a turning function algorithm. This is done to prevent excessive heating of the material which can occur due to the increased energy density at these turning points. In a study carried out with the Arcam S12 system [28], it was suggested that the reduction in energy density due to the turning function resulted in porosity concentrated at the boundaries of the hatched area. It is possible that the distribution of unconsolidated material presented here can also be attributed to an excessive increase in beam speed applied by this turning function algorithm such that the energy density applied at this location is insufficient to achieve complete melting.

Specimens produced using the cathode based Arcam Q10 system, tested under four point bend conditions with a similar build/loading orientation, show superior fatigue properties to those produced in the present study [39]. The most notable difference in the scanning techniques used in this work is the use of a *Theme* assignment, rather than the *Model* assignment used in the present work. Under the *Theme* assignment, *hatching* passes are defined for all parts over the build area with turning points occurring at the extremities of the build area for a given layer. Under this assignment, turning points are not confined to to individual parts, such as is the case for *Model* assignment, which could have alleviated the high density LOF occurring for every part in the build.

5. Conclusions

In this study the influence of finish machining and post-built HIP treatments on defect population and fatigue behaviour has been investigated using a four point bend test method to determine their effectiveness for enhancing the fatigue life of Ti-6Al-4V specimens produced using the Arcam Q20 plus SEBM system. The following conclusions were reached:

- At shallow machining depths (<1.00 mm), the fatigue response of the material varied significantly based on material removal depth. This was due to the heterogeneity in LOF defect distribution near the as-built part surface.
- Stress concentration due to the presence of LOF defects was attributed to be the predominant cause for limited fatigue performance in both HIP'ed and non-HIP'ed material. LOF defects were found to be concentrated in a band of material located in the sub-surface of as-built material. The location of which corresponds to the turning point of each hatched path. This suggests that the increase in beam speed applied by the turning function algorithm during *hatching* could be the reason for insufficient melting at this location.
- Removal of a sufficient depth of material (>1.00 mm) during post-build finish machining has been shown to improve fatigue performance through the removal defect rich material, concentrated in the sub-surface of each specimen. In specimens which were machined to these conditions, cracks were found to initiate at LOF defects exposed at machined surface rather than in the sub-surface. Removal of less material (<0.50 mm) during machining was not shown to result in a similar performance improvement. Rather, defects were brought in closer proximity to the surface of the specimen subject to maximum stress.
- Surface exposure and interconnected ligaments between LOF defects resulted in the HIP treatment being ineffective at healing harmful near-surface LOF porosity. Despite this, a fatigue performance improvement was observed following HIP, which was attributed to a reduction in the volume of gas porosity.

Declaration of competing interests

The authors declare that they have no known competing financial interests or personal relationships that could have appeared to influence the work reported in this paper.

Acknowledgments

This study was funded by the EPSRC Industrial Doctorate Centre in Machining Science (EP/L016257/1) and MAPP the EPSRC Future Manufacturing Hub in Manufacture using Advanced Powder Processes (EP/P006566/1) as well as Seco Tools and Element Six. The authors would also like to acknowledge the Henry Royce Institute for Advanced Materials, funded through EPSRC grants EP/R00661X/1, EP/S019367/1, EP/P02470X/1 and EP/P025285/1, for the financial support and EBM-ARCAM Q20 access at Royce@Sheffield. Finally, the authors would like to acknowledge Dr. Vahid Nekouie and the Henry Royce Institute for their support in carrying out the HIP treatment of the specimens tested in this study.

References

[1] W. Harun, N. Manam, M. Kamariah, S. Sharif, A. Zulkifly, I. Ahmad, H. Miura, A review of powdered additive manufacturing techniques for Ti-6Al-4V biomedical applications, Powder Technology 331 (2018) 74–97. doi:10.1016/j.powtec.2018.03.010.

[2] S. Gorsse, C. Hutchinson, M. Gouné, Additive manufacturing of metals : a brief review of the characteristic microstructures and properties of steels , Ti-6Al-4V and high-entropy alloys, Science and Technology of Advanced Materials 18 (1) (2017) 584–610. doi:10.1080/14686996.2017.1361305.

[3] T. Childerhouse, M. Jackson, Near Net Shape Manufacture of Titanium Alloy Components from Powder and Wire: A Review of State-of-the-Art Process Routes, Metals 9 (6) (2019) 689. doi:10.3390/met9060689.

[4] P. C. Priarone, G. Ingarao, R. Lorenzo, L. Settineri, Influence of Material-Related Aspects of Additive and Subtractive Ti-6Al-4V Manufacturing on Energy Demand and Carbon Dioxide Emissions, Journal of Industrail Ecology 21 (2016) 191–202. doi:10.1111/jiec.12523.

[5] L. Nickels, AM and aerospace : an ideal combination, Metal Powder Report 70 (6) (2015) 300–303. doi:10.1016/j.mprp.2015.06.005.

[6] E. Uhlmann, R. Kersting, T. B. Klein, M. F. Cruz, A. V. Borille, Additive Manufacturing of Titanium Alloy for Aircraft Components, Procedia CIRP 35 (2015) 55–60. doi:10.1016/j.procir.2015.08.061.

[7] A. H. Chern, P. Nandwana, T. Yuan, M. M. Kirka, R. R. Dehoff, P. K. Liaw, C. E. Duty, A review on the fatigue behavior of Ti-6Al-4V fabricated by electron beam melting additive manufacturing, International Journal of Fatigue 119 (2019) 173 – 184. doi:https://doi.org/10.1016/j.ijfatigue.2018.09.022.

[8] L.-c. Zhang, Y. Liu, S. Li, Y. Hao, Additive Manufacturing of Titanium Alloys by Electron Beam Melting : A Review, Advanced Engineering Materials 1700842 (2018) 1–16. doi:10.1002/adem.201700842.

[9] C. Körner, Additive manufacturing of metallic components by selective electron beam melting a review, International Materials Reviews 6608 (May). doi:10.1080/09506608.2016.1176289.

[10] M. Galati, P. Minetola, G. Rizza, Surface roughness characterisation and analysis of the Electron Beam Melting (EBM) process, Materials 12 (13). doi:10.3390/ma12132211.

[11] X. Gong, J. Lydon, K. Cooper, K. Chou, Beam speed effects on Ti-6Al-4V microstructures in electron beam additive manufacturing, Journal of Materials Research 29 (17) (2014) 1951–1959. arXiv:1004.4715, doi:10.1557/jmr.2014.125.

[12] F. Caiazzo, F. Cardaropoli, V. Alfieri, V. Sergi, L. Cuccaro, Experimental analysis of selective laser melting process for Ti-6Al-4V turbine blade manufacturing, XIX International Symposium on High-Power Laser Systems and Applications 86771 (January 2013) (2013) 86771H. doi:10.1117/12.2010577.

[13] P. Edwards, A. O'Conner, M. Ramulu, Electron Beam Additive Manufacturing of Titanium Components : Properties and Performance, Journal of Manufacturing Science and Engineering 135 (December 2013) (2013) 061016–1–061016–7. doi:10.1115/1.4025773.

[14] A. Safdar, H. Z. He, L. Y. Wei, A. Snis, L. E. Chavez De Paz, Effect of process parameters settings and thickness on surface roughness of EBM produced Ti-6Al-4V, Rapid Prototyping Journal 18 (5) (2012) 401–408. doi:10.1108/13552541211250391.

[15] S. S. Kumar, S. S. Hiremath, A Review on Abrasive Flow Machining (AFM), Procedia Technology 25 (2016) 1297–1304. doi:10.1016/j.protcy.2016.08.224.

[16] J. Sambharia, H. S. Mali, Recent developments in abrasive flow finishing process: A review of current research and future prospects, Proceedings

of the Institution of Mechanical Engineers, Part B: Journal of Engineering Manufacture 233 (2) (2019) 388–399. doi:10.1177/0954405417731466.

[17] A. Dolimont, E. Rivière-Lorphèvre, F. Ducobu, S. Backaert, Impact of chemical polishing on surface roughness and dimensional quality of electron beam melting process (EBM) parts, AIP Conference Proceedings 1960 (May 2018). doi:10.1063/1.5034999.

[18] A. Mohammad, M. K. Mohammed, A. M. Alahmari, Effect of laser ablation parameters on surface improvement of electron beam melted parts, International Journal of Advanced Manufacturing Technology 87 (1-4) (2016) 1033–1044. doi:10.1007/s00170-016-8533-4.

[19] J. J. Lewandowski, M. Seifi, Metal Additive Manufacturing: A Review of Mechanical Properties, Annual Review of Materials Research 46 (1) (2016) 151–186. doi:10.1146/annurev-matsci-070115-032024.

[20] A. Mohammadhosseini, D. Fraser, S. H. Masood, M. Jahedi, Microstructure and mechanical properties of Ti-6Al-4V manufactured by electron beam melting process, Material Research Innovations 17 (December) (2013) 106–112. doi:10.1179/1432891713Z.000000000302.

[21] H. Galarraga, D. A. Lados, R. R. Dehoff, M. M. Kirka, P. Nandwana, Effects of the microstructure and porosity on properties of Ti-6Al-4V ELI alloy fabricated by electron beam melting (EBM), Additive Manufacturing 10 (2016) 47–57. doi:https://doi.org/10.1016/j.addma.2016.02.003.

[22] X. Shui, K. Yamanaka, M. Mori, Y. Nagata, A. Chiba, Effects of post-processing on cyclic fatigue response of a titanium alloy additively manufactured by electron beam melting, Materials Science & Engineering A 680 (August 2016) (2017) 239–248. doi:10.1016/j.msea.2016.10.059.

[23] S. Tammas-Williams, P. Withers, I. Todd, P. Prangnell, The Influence of Porosity on Fatigue Crack Initiation in Additively Manufactured Titanium Components, Scientific Reports 7 (2017) 7308. doi:https://doi.org/10.1038/s41598-017-06504-5.

[24] R. Cunningham, S. P. Narra, T. Ozturk, J. Beuth, A. D. Rollett, Evaluating the Effect of Processing Parameters on Porosity in Electron Beam Melted Ti-6Al-4V via Synchrotron X-ray Microtomography, JOM 68 (3) (2016) 765–771. doi:10.1007/s11837-015-1802-0.

[25] S. Tammas-Williams, P. Withers, I. Todd, P. Prangnell, The Effectiveness of Hot Isostatic Pressing for Closing Porosity in Titanium Parts Manufactured by Selective Electron Beam Melting, Metallurgical and Materials Transactions 47 (2016) 1939–1946. doi:https://doi.org/10.1007/s11661-016-3429-3.

[26] H. Masuo, Y. Tanaka, S. Morokoshi, H. Yagura, T. Uchida, Y. Yamamoto, Y. Murakami, Effects of Defects, Surface Roughness and HIP on Fatigue Strength of Ti-6Al-4V manufactured by Additive Manufacturing, Procedia Structural Integrity 7 (2017) 19 – 26, 3rd International Symposium on Fatigue Design and Material Defects, FDMD 2017. doi:https://doi.org/10.1016/j.prostr.2017.11.055.

[27] L. Facchini, A. Molinari, Microstructure and mechanical properties of Ti-6Al-4V produced by electron beam melting of pre-alloyed powders, Rapid Prototyping Journal 3 (February) (2009) 171–178. doi:10.1108/13552540910960262.

[28] S. Tammas-Williams, H. Zhao, F. Léonard, F. Derguti, I. Todd, P. B. Prangnell, XCT analysis of the influence of melt strategies on defect population in Ti-6Al-4V components manufactured by Selective Electron Beam Melting, Materials Characterization 102 (2015) 47–61. doi:10.1016/j.matchar.2015.02.008.

[29] N. Hrabe, T. Gnäupel-Herold, T. Quinn, Fatigue properties of a titanium alloy (Ti-6Al-4V) fabricated via electron beam melting (EBM): Effects of internal defects and residual stress, International Journal of Fatigue 94 (2017) 202 – 210. doi:https://doi.org/10.1016/j.ijfatigue.2016.04.022.

[30] ASTM International, ASTM Standard F2924: Standard specification for additive manufacturing titanium-6 aluminum-4 vanadium with powder bed fusion, in: ASTM book of standards, West Conshohocken, PA, 2014.

[31] R. Cunningham, A. Nicolas, J. Madsen, E. Fodran, M. D. Sangid, A. D. Rollett, R. Cunningham, A. Nicolas, J. Madsen, E. Fodran, M. D. Sangid, A. D. Rollett, Analyzing the effects of powder and post- processing on porosity and properties of electron beam melted Ti-6Al-4V, Materials Research Letters 5 (7) (2017) 516–525. doi:10.1080/21663831.2017.1340911.

[32] M. Seifi, A. Salem, D. Satko, J. Shaffer, J. J. Lewandowski, Defect distribution and microstructure heterogeneity effects on fracture resistance and fatigue behavior of EBM Ti-6Al-4V, International Journal of Fatigue 94 (2017) 263–287. doi:10.1016/j.ijfatigue.2016.06.001.

[33] A. Cox, S. Herbert, J.-P. Villain-Chastre, S. Turner, M. Jackson, The effect of machining and induced surface deformation on the fatigue performance of a high strength metastable β titanium alloy, International Journal of Fatigue 124 (February) (2019) 26–33. doi:10.1016/j.ijfatigue.2019.02.033.

[34] D. Suárez Fernández, B. Wynne, P. Crawforth, K. Fox, M. Jackson, The effect of forging texture and machining parameters on the fatigue performance of titanium alloy disc components, International Journal of Fatigue 142 (2021) 105949. doi:https://doi.org/10.1016/j.ijfatigue.2020.105949.

[35] T. Childerhouse, Defect characterisation on SEBM fracture surfaces, https://github.com/TChilderhouse/Defect-characterisation-on-SEBM-fracture-surfaces (2021).

[36] Y. Murakami, Material defects as the basis of fatigue design, International Journal of Fatigue 41 (2012) 2–10. doi:10.1016/j.ijfatigue.2011.12.001.

[37] Y. Murakami, K. J. Miller, What is fatigue damage ? A view point from the observation of low cycle fatigue process, International Journal of Fatigue 27 (2005) 991–1005. doi:10.1016/j.ijfatigue.2004.10.009.

[38] D. Greitemeier, F. Palm, F. Syassen, T. Melz, Fatigue performance of additive manufactured Ti-6Al-4V using electron and laser beam melting, International Journal of Fatigue 94 (2017) 211–217. doi:10.1016/j.ijfatigue.2016.05.001.

[39] A. H. Chern, P. Nandwana, R. Mcdaniels, R. R. Dehoff, P. K. Liaw, R. Tryon, C. E. Duty, Materials Science & Engineering A Build orientation , surface roughness , and scan path influence on the microstructure , mechanical properties , and flexural fatigue behavior of Ti – 6Al – 4V fabricated by electron beam melting, Materials Science & Engineering A 772 (November 2019) (2020) 138740. doi:10.1016/j.msea.2019.138740.